PHYSICAL REVIEW FLUIDS **7**, 104609 (2022)

Influence of Prandtl number in turbulent Rayleigh-Bénard convection over rough surfaces

Mukesh Sharma, Krishan Chand, and Arnab Kr. De*

Department of Mechanical Engineering, Indian Institute of Technology Guwahati, Assam, 781039 India

(Received 14 June 2022; accepted 4 October 2022; published 26 October 2022)

The present study numerically investigates the effect of the Prandtl number ($0.1 \leqslant \mathrm{Pr} \leqslant 100$) on the flow structures and heat transport mechanism in a two-dimensional rectangular rough cell of aspect ratio 2, for more than 2 decades of the Rayleigh number ($10^7 \leqslant \mathrm{Ra} \leqslant 5 \times 10^9$). Large-scale diffuse structures transform into finer ones with increase in either Ra or Pr. The height of roughness elements relative to the thermal boundary layer (TBL) thickness establishes the level of perturbations introduced into the system. A stronger thermal forcing or larger Pr facilitates a thinner TBL, which triggers a quicker response from the elements in the emission of plumes. In comparison to the smooth case, heat transport is enhanced significantly with the introduction of roughness. The near invariance of the Nusselt number Nu with Pr in smooth cells is overcome in the rough cell, where a monotonically increasing heat flux is obtained. A greater presence of plumes in the domain is identified by an augmented volume fraction and thermal dissipation from plumes. The flow intensity measured in terms of the global Reynolds number Re shows significant improvement for $10^8 \leqslant \mathrm{Ra} \leqslant 5 \times 10^9$ and $5 \leqslant \mathrm{Pr} \leqslant 100$ in comparison to the smooth case.

DOI: 10.1103/PhysRevFluids.7.104609

I. INTRODUCTION

Thermal convection is ubiquitous in nature and finds its application in various industrial and engineering applications. Rayleigh-Bénard convection (RBC), the bottom-heated and top-cooled configuration, is a paradigmatic model [1–3] widely used to study thermal convection, where fluid sets in motion when the temperature difference ΔT between the horizontal plates is sufficiently high, enabling buoyant force to overcome viscous and thermal diffusion. With ΔT being significantly high, there is an emergence of fascinating flow structures, which play a tremendous role in controlling the vertical heat transfer rate and the associated mechanism in the convection cell.

The dynamics of RBC is mainly dictated by two nondimensional parameters, the Rayleigh number ($\mathrm{Ra} = \beta g \Delta T H^3/\nu\alpha$), and the Prandtl number ($\mathrm{Pr} = \nu/\alpha$), where β is the isobaric thermal expansion coefficient, g is the acceleration due to gravity, H is the height of the convection cell, ν is the kinematic viscosity, and α is the thermal diffusivity of the fluid. While Ra specifies the magnitude of the thermal forcing, Pr denotes the strength of the momentum diffusivity relative to the thermal diffusivity. A fundamental issue in thermal convection is to determine how the global heat transfer efficiency, given in terms of a nondimensional parameter, the Nusselt number Nu, specifying the relative contribution of convection over conduction, behaves in response to the input control parameters, Ra and Pr.

In addition to Ra, Pr has a strong effect on the prevalent dominating flow structures and the heat transfer mechanism [4–6]. Verzicco and Camussi [7] demarcated two types of flow regimes in their

---

[*] Author to whom correspondence should be addressed: akd@iitg.ac.in

study inside a cylindrical cell covering $0.022 \leqslant \mathrm{Pr} \leqslant 15$ for $\mathrm{Ra} \leqslant 2 \times 10^7$. The first regime was observed for $\mathrm{Pr} \leqslant 0.35$, where large-scale circulation (LSC) dominates and is the major benefactor in vertical heat transfer. Owing to the remarkable contributions, LSC is considered as the "engine" for low-Pr convection. Also, in this case, Nu was found to increase with Pr. The second regime was observed for $\mathrm{Pr} > 0.35$, where thermal plumes emerge as the major contributor in heat transfer and the role of large-scale circulation is largely diminished. Here, Nu becomes independent of Pr with the scaling exponent being 2/7. In general, for low-Pr fluids, a thicker thermal boundary layer (TBL) is formed, due to which there is more of a tendency for diffusive heat transfer and hence fewer and weak plume structures are formed. However, with an increase in Pr, the thermal boundary layer becomes thinner, favoring the formation of a greater number of stronger and finer plumes.

Malevsky [8] also highlighted the influence of Pr by observing the probability density function (PDF) of θ fluctuation along with its spectra. For low Pr, the increasing dominance of large-scale structures with decreasing Pr leads to the Gaussian-like skirt of the PDFs, while at high Pr, the emergence of small-scale structures in the form of isolated fine plumes is responsible for the exponential-like shape. The above observation is in line with those of Yakhot [9] and Solomon and Gollub [10,11], who credited the predominance of large-scale structures in giving Gaussian shape to the PDFs while small-scale structures enforce the exponential shape. The spectra of temperature fluctuations measured at different horizontal planes also revealed the Pr dependence, and they were found to be steeper with decreasing Pr. Another interesting feature discovered by Malevsky [8] is the increasing tendency for inverse kinetic energy transfer with the amplification of Pr. The same was manifested from the steeper kinetic energy spectra at higher Pr with the slope of the inertial subrange being close to $-11/5$ (Bolgiano and Obukhov (BO59) scaling [12,13]). In the literature, BO59 scaling has been shown to be closely connected to the inverse energy transfer [14,15].

Huang and Zhou [16] in their two-dimensional (2D) study reported an anomalous Nu(Pr) relation in comparison to a 3D cylindrical case for a moderate $\mathrm{Ra} \leqslant 10^9$ and $\mathrm{Pr} \approx 2$–3 range, where Nu settles for a minimum value rather than attaining maxima as in the 3D case. The reason for the anomaly was attributed to the competition between the corner rolls and LSC creating countergradient heat transport, which is a striking feature of 2D convection as the fluid lacks the third direction to escape. Furthermore, heat transfer dependency on Pr was found to diminish with increasing Pr. At higher values of Ra, $\mathrm{Ra} \geqslant 3 \times 10^9$, Pr dependency was qualitatively similar to that observed for the 3D case. Yang *et al.* [17] also obtained a lack of Pr dependence in the heat transfer rate for their experimental investigation inside a cylindrical cell for $2.63 \times 10^8 \leqslant \mathrm{Ra} \leqslant 3.89 \times 10^{10}$ and $3.58 \leqslant \mathrm{Pr} \leqslant 9.40$. However, the Reynolds number Re showed significant dependence on Pr ($\mathrm{Re} = \mathrm{Ra}^{0.47}\mathrm{Pr}^{-0.72}$) such that its value dropped with an increase in Pr. They also observed that the local temperature fluctuations weaken with increasing Pr.

van der Poel *et al.* [18] also highlighted the similar behavior of Nu(Pr) in 2D and 3D cases for a large Pr, where Nu data for both the cases converged. The largest difference in Nu is seen at intermediate Pr, which is associated with the difference in LSC dynamics in 2D and 3D cases. In the 2D case, there is an emergence of a stronger LSC with corner rolls, whereas in the 3D case, LSC is less pronounced with smaller rolls. They also observed the Pr dependence of the global Re, where the flow strength was observed to be monotonically decreasing with growing Pr such that it is always higher for 2D than 3D. However, for a higher Pr, the Re for both 2D and 3D converged, which again highlights similar behavior in the two modes. Pandey *et al.* [19] reported the similarities between 2D and 3D for large Pr convection. On observing the first ten most dominant Fourier modes, close resemblances between 2D and 3D convection were revealed. Similar scaling for kinetic [$E_u(k) \sim k^{-13/3}$] and temperature spectra ($\sim k^{-2}$) further highlighted that the behavior in the two cases is alike. Li *et al.* [20] experimentally investigated the effect of Pr on heat transport and flow structures in a quasi-2D rectangular convection cell for $6 \times 10^8 \leqslant \mathrm{Ra} \leqslant 3 \times 10^{10}$ and $11.7 \leqslant \mathrm{Pr} \leqslant 650.7$. It was observed that a well-defined LSC exists for Pr up to 145.7. In this range, the increase in Pr is accompanied by a lesser number of thermal plumes traversing through the central region of the cell. For the two extremes, $\mathrm{Pr} = 345.2$ and $\mathrm{Pr} = 650.7$, LSC disappears, and in place of that, slender thermal plumes that move randomly in the cell emerge. The breakdown of LSC also resulted in a regime transition in the Re(Ra, Pr) scaling law.

With the exceptional potential illustrated by various roughness studies [21–25] in RBC to achieve the asymptotic heat transfer scaling [26,27], there has been an increased interest in capitalizing on this enhanced understanding to achieve incessant $1/2$ scaling and to emulate and understand real-life flows occurring in nature. To do so, studies with multiscale roughness [24,25,28], as opposed to simplified monoscale roughness, are gaining popularity owing to their ability to sustain the local $1/2$ scaling for a wider Ra range and also elicit a response similar to what may be observed in real-life flows.

The efficacy of a roughened surface is dependent on its geometric parameters [22,24,29], the height and the width of a roughness element. A height of the roughness elements that is comparable to the TBL is known to yield enhancement in heat transfer. However, when the TBL is too thick such that roughness elements are submerged beneath it, suppression of the heat transfer rate is observed. Similarly, a width of the roughness elements that is too narrow or wide reveals flow characteristics similar to those observed in a smooth surface. A major deduction is that to obtain a maximized heat transfer rate, optimization or tuning of the geometric parameters is required, which explains the role played by the selection of the roughness geometry and its parameters. The present work employs an irregular multiscale triangular roughness with an emphasis on facilitating a natural selection of the roughness elements so that the roughness mimics the roughnesses observed in real life, even though it is 2D.

Zhang *et al.* [29] simulated 2D flow with uniform triangular roughness for $10^7 \leqslant \mathrm{Ra} \leqslant 10^{11}$ with constant $\mathrm{Pr} = 1$. It was reported that it takes a critical height h_c of the roughness elements to realize enhancement in heat transport. Below h_c, rough surfaces inhibit heat transport. However, h_c was observed to decrease with Ra, which explains the prevalence of augmentation of the heat transfer rate at higher Ra. Toppaladoddi *et al.* [22], using optimized roughness parameters for sinusoidal roughness in a 2D cell of double aspect ratio, obtained a heat transfer scaling exponent of 0.483 for $4 \times 10^6 \leqslant \mathrm{Ra} \leqslant 3 \times 10^9$. They interpreted it as the attainment of the ultimate scaling. However, Zhu *et al.* [23] refuted the above claim by exploring a wider $10^8 \leqslant \mathrm{Ra} \leqslant 10^{12}$ range. They reported that the roughness-facilitated $1/2$ scaling is temporary, and the classical $1/3$ scaling returns at a higher Ra range. To overcome the saturation of the much-sought-after $1/2$ scaling, Zhu *et al.* [24] introduced three scales of roughness. The above provision allowed them to sustain $1/2$ scaling for a wider Ra range, $10^8 \leqslant \mathrm{Ra} \leqslant 10^{11}$. It was hypothesized that different roughness length scales introduce thermal boundary layer perturbations at different Ra. Large-scale elements are activated at a lower Ra, while smaller elements require a larger thermal forcing to assist enhancement in heat transport. To investigate the influence of the spatial arrangement of roughness elements on the heat transport mechanism and flow structures, Dong *et al.* [30] performed 2D simulations in a square cavity with rough horizontal walls. They observed that the Nu scaling exponent varies depending on how the roughness elements are populated (dense or sparse). However, the Reynolds number was observed to be insensitive to the spatial arrangement in the employed roughness models.

Xie and Xia [31] experimentally explored the influence of Pr on Nu(Ra) scaling in a cylindrical rough cell with periodically distributed pyramid-shaped elements for $7.5 \times 10^7 \leqslant \mathrm{Ra} \leqslant 1.31 \times 10^{11}$ and $3.57 \leqslant \mathrm{Pr} \leqslant 23.34$. They classified the flow into three regimes based on Nu(Ra) scaling. Regime I experienced no influence of the roughness on Nu(Ra), whereas regimes II and III revealed enhanced heat transport scaling. The transition from regime I to regime II happens with the TBL becoming thinner than the roughness height, whereas the transition from regime II to regime III is accompanied by the viscous boundary layer (BL) becoming thinner than the roughness height. Furthermore, they reported that the larger the Pr is, the greater enhancement in heat transfer is possible when a larger aspect ratio of the roughness elements is considered. The reason for the same was anticipated to be linked with the stronger clustering of thermal plumes.

Recently, Yang *et al.* [32], while working with a 2D square rough cell, observed the effect of Pr on the critical height h_c of the roughness elements above which an enhancement in heat transfer with respect to a smooth cell can be obtained. They explored $10^7 \leqslant \mathrm{Ra} \leqslant 10^9$ and $0.01 \leqslant \mathrm{Pr} \leqslant 100$,

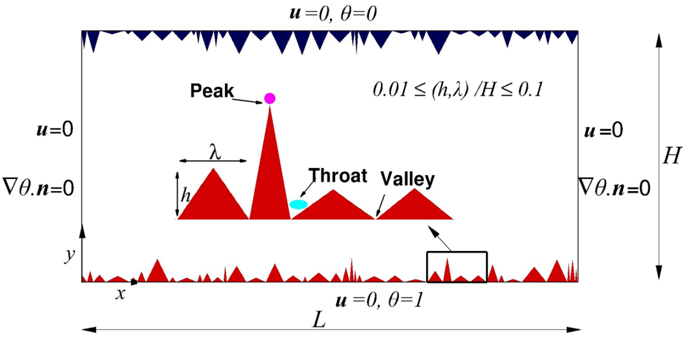

FIG. 1. Schematic of the 2D rectangular convection cell featuring irregular triangular roughness on the horizontal plates. A blown-up view of a small portion of the bottom plate depicts peak, throat, and valley regions associated with the roughness elements. Here, h and λ are the height (amplitude) and width (wavelength) of the roughness elements, respectively.

where $h_c(\mathrm{Pr})$ revealed three distinct regimes. The regime at low Pr dominated by LSC shows a decrement of h_c with increasing Pr. The regime at moderate Pr, characterized by strong competition between the corner rolls and the LSC with the advent of thermal plumes, experiences an increment of h_c with the magnified Pr. Lastly, the regime at high Pr features fine plumes with the weakening of the large-scale flows, where h_c follows a decreasing trend with Pr. To the best of our knowledge, the effect of Pr in a multiscale roughness setup has not been explored, which calls for an in-depth study exploring how flow structures evolve and are altered at different Ra and Pr in the rough cell.

The remainder of this paper is organized in the following manner. Section II provides details about the problem setup and the numerical method used, while Sec. III includes a discussion of the Nusselt number scaling law, the effect of Pr on the heat transport mechanism, the plume statistics, and the flow intensity. The results for both smooth and rough cells are discussed appropriately. However, the major emphasis is laid on the roughened cell while elucidating the flow behavior for varying Pr and Ra. Lastly, the findings of this paper are summarized in Sec. IV.

II. NUMERICAL DETAILS

Governing nondimensional transport equations for incompressible, buoyancy-driven flows in the spirit of Boussinesq approximation are obtained as

$$\frac{\partial u_i}{\partial x_i} = 0, \tag{1}$$

$$\frac{\partial u_i}{\partial t} + \frac{\partial (u_i u_j)}{\partial x_j} = -\frac{\partial p}{\partial x_i} + \sqrt{\frac{\mathrm{Pr}}{\mathrm{Ra}}}\frac{\partial^2 u_i}{\partial x_j \partial x_j} + \theta \delta_{ib}, \tag{2}$$

$$\frac{\partial \theta}{\partial t} + \frac{\partial (u_j \theta)}{\partial x_j} = \frac{1}{\sqrt{\mathrm{Ra}\,\mathrm{Pr}}}\frac{\partial^2 \theta}{\partial x_j \partial x_j}, \tag{3}$$

where $u_i = (u, v)$ is the velocity in the Cartesian direction $x_i = (x, y)$, $\theta = (T - T_C)/(T_H - T_C)$ is the nondimensional temperature where T_H and T_C are the temperatures of the bottom and top plates, respectively, p is the pressure, b is the buoyancy direction, and δ is the Kronecker delta. The above set of equations are nondimensionalized using reference scales for length, velocity, temperature, and time as vertical height H, free-fall velocity $\sqrt{\beta g \Delta T H}$, $\Delta T = T_H - T_C$, and $(H/\beta g \Delta T)^{1/2}$, respectively. All the simulations are carried out in a 2D rectangular cell of aspect ratio $\Gamma = L/H = 2$ covering $10^7 \leqslant \mathrm{Ra} \leqslant 5 \times 10^9$ for $0.1 \leqslant \mathrm{Pr} \leqslant 100$. Figure 1 shows a schematic diagram of the convection cell with the applied boundary conditions and the detailed roughness geometry implanted on the top and bottom plates. The horizontal plates consist of irregular rough surfaces with triangular elements. All the walls admit the no-slip velocity boundary condition. While the lateral walls are kept adiabatic, the top and bottom horizontal plates are maintained at constant temperatures.

The height h and width λ of the roughness elements, as shown in Fig. 1, are generated using a standard random number generator with uniform distribution. Both h and λ are set to vary independently such that they scale between 1 and 10% of the cell height. Though the base and height of an element are arbitrarily chosen, the present roughness setup cannot accommodate all possible combinations of λ and h owing to the finite axial length of the convection cell, which is an essential feature of truly random roughness. Thus the present roughness setup can be interpreted as irregular multiscale roughness which is random only to a limited extent. Note that the effective height ($H_{\text{eff}} = V_{\text{fluid}}/L$) of the convection cell, as described by Zhu *et al.* [24], is taken as the characteristic length scale while describing Ra for the rough cases.

A nonstaggered finite-volume method in conjunction with the diffuse-interface immersed boundary method (DIIBM) [33] is used to solve the governing conservation laws. While the nonlinear convective terms are approximated using the second-order Adams-Bashforth scheme, the buoyancy, pressure, and diffusive terms are treated using the second-order Crank-Nicolson scheme. A two-step predictor-corrector technique is employed in the solver. In the first step, the provisional velocity field is calculated using the known pressure field, and in the second step, it is corrected by solving the Poisson equation, which enforces mass balance indirectly. All the resulting sparse linear systems are solved using the biconjugate gradient stabilized method (BiCGSTAB) preconditioned by a highly scalable block-diagonal version of the modified strongly implicit (MSI) procedure. To speed up the computation, the standard message-passing interface (MPI) libraries are used for parallelization of the solver. Further details of the numerical technique are given by Peter and De [34] and De *et al.* [35]. Note that the present numerical setup has been used for a number of complex flows that involve stationary [28,36,37] and moving boundaries [38,39].

A grid that is uniform in the horizontal direction and nonuniform in the vertical direction is employed such that the regions close to rough surfaces are resolved sufficiently. For adequate spatial resolution, the Kolmogorov length scale [$\eta \approx \text{Pr}^{1/2}/(\text{Ra}\,\text{Nu})^{1/4}$] is resolved. Also, grid independence of the simulations, which is discussed later, is ensured for the accuracy of the results. In Table I, details of the simulation parameters are listed for the rough cases. Note that we have also performed adequately resolved simulations for the smooth case for the same input parameters to enable a direct comparison with the rough cases. From Table I, it can be observed that for $\text{Pr} = 0.1$ cases, the flow adequately resolves the Kolmogorov length scale such that for the most demanding case, $\text{Ra} = 5 \times 10^9$, $\Delta x_{\max}/\eta$ and $\Delta y_{\max}/\eta$ are 0.97 and 1, respectively. For $\text{Pr} \geqslant 1$ cases, the resolutions in the horizontal and vertical directions are kept at at least 0.85 times the Kolmogorov length scale. Note that the reference Nusselt number for calculation of η is taken from Chand *et al.* [28]. For temporal resolution, the time increment Δt is chosen in such a way that it is smaller than the Kolmogorov time scale [$\eta_\tau = \sqrt{\text{Pr}/(\text{Nu} - 1)}$] and the maximum Courant number is always less than 0.2. For the most demanding case ($\text{Ra} = 5 \times 10^9$ and $\text{Pr} = 0.1$), the ratio $\Delta t/\eta_\tau$ is as small as 8.78×10^{-6}, and it never exceeds 0.01 for all simulations. The simulations are started from the conduction state, and once a statistically stationary state is reached, sampling of the data is carried out.

To check the effect of resolution on the solution, four progressively refined meshes (M_i, $i = 1$–4) are tested for convergence of global Nu, and variance of temperature fluctuations, $\langle \sigma_\theta^2 \rangle_V$, at $\text{Ra} = 5 \times 10^9$ for $\text{Pr} = 1$ and 100. The global Nusselt number and variance are calculated as $\langle \text{Nu} \rangle_{V,t} = \sqrt{\text{Ra}\,\text{Pr}} \langle v\theta \rangle_{V,t} - \langle \partial_y \theta \rangle_{V,t}$ and $\langle \sigma_\theta^2 \rangle_V = \langle \langle \theta(\boldsymbol{x}, t)^2 \rangle_t - \langle \theta(\boldsymbol{x}, t) \rangle_t^2 \rangle_V$. The details of the mesh refinement study are listed in Table II. It can be observed that for the $\text{Pr} = 1$ case, the maximum variation in $\langle \text{Nu} \rangle_{V,t}$ and $\langle \sigma_\theta^2 \rangle_V$ between any two successive grids does not exceed 1.4 and 7.6%, respectively. For $\text{Pr} = 100$, the maximum variation is 1.76 and 7.2% in $\langle \text{Nu} \rangle_{V,t}$ and $\langle \sigma_\theta^2 \rangle_V$, respectively. A slightly higher variance of higher-order moments is also observed by Toppaladoddi *et al.* [25] while considering different flow realizations with fractal roughness. Note that mesh M_3,

TABLE I. Details of simulation parameters for different Ra cases. Starting from the left, Pr is the Prandtl number, N_x and N_y are the grid resolution in the x and y directions, $\Delta x_{\max}/\eta$ and $\Delta y_{\max}/\eta$ are the ratio of the maximum grid spacing in x and y directions, respectively, to the Kolmogorov length scale [$\eta \approx \mathrm{Pr}^{1/2}/(\mathrm{Ra\,Nu})^{1/4}$], and $\langle \mathrm{Nu} \rangle_{V,t}$ is the calculated global Nusselt number. Note that for Pr $\geqslant$ 1, the Nu is listed for the increasing order of Pr, i.e., for Pr = 1, 5, 10, 20, 50, 100, respectively.

Pr	$N_x \times N_y$	$\Delta x_{\max}/\eta$	$\Delta y_{\max}/\eta$	$\langle \mathrm{Nu} \rangle_{V,t}$
		Ra = 10^7		
0.1	1321 × 1081	0.49	0.43	10.5
$\geqslant$1	1001 × 601	0.20	0.25	(10.9,13.75,15.52, 17.31,18.86,19.31)
		Ra = 10^8		
0.1	1561 × 1081	0.85	0.89	23.64
$\geqslant$1	1201 × 601	0.38	0.55	(27.40,31.57,38.32, 39.15,44.60,47.2)
		Ra = 10^9		
0.1	3241 × 2281	0.84	0.86	55.02
$\geqslant$1	2041 × 1081	0.52	0.70	(77.34,81.21,90.28, 101.135,114.05,120.65)
		Ra = 5×10^9		
0.1	4681 × 3241	0.97	1	105.57
$\geqslant$1	2521 × 1561	0.73	0.85	(147.63,165.28,170.161, 177.36,190.21,204.05)

the chosen one for the simulations, is a perfect blend of adequate spatial resolution and accuracy of the solution. The mesh refinement study clearly establishes the employment of requisite spatial resolution of the flow field along with the robustness of the current numerical setup. Further details of the numerical setup, which include comparison tests, different flow realizations, and the near-wall resolution, can be found in the Appendix.

III. RESULTS AND DISCUSSION

In the following, we discuss the quantification of the vertical heat transfer by Nu and its dependence on Ra and Pr in Sec. III A, followed by identification of the prevalent heat transfer mechanism for different sets of input parameters, Ra and Pr, in Sec. III B. The increased presence of plumes in the rough cells is recorded from the augmented volume fraction of plumes in Sec. III C, which is followed by quantification of flow strength and its dependence on input parameters in Sec. III D. Note that to present our argument, a number of ensemble averages of a random variable

TABLE II. Details of the grid independence study performed at Ra = 5×10^9 for Pr = 1 and 100. Here, M_3 is the adopted mesh, $N_x \times N_y$ is the grid resolution, $\langle \mathrm{Nu} \rangle_{V,t}$ is the calculated mean Nusselt number, and $\langle \sigma_\theta^2 \rangle_V$ is the global variance of temperature fluctuations.

		Pr = 1		Pr = 100	
Mesh M_i	$N_x \times N_y$	$\langle \mathrm{Nu} \rangle_{V,t}$	$\langle \sigma_\theta^2 \rangle_V$ ($\times 10^{-3}$)	$\langle \mathrm{Nu} \rangle_{V,t}$	$\langle \sigma_\theta^2 \rangle_V$ ($\times 10^{-4}$)
M_1	2101 × 1381	147.12	2.36	200.64	7.036
M_2	2301 × 1453	149.18	2.318	200.52	6.832
M_3	**2521 × 1561**	**147.63**	**2.494**	**204.05**	**7.324**
M_4	2771 × 1681	148.64	2.389	203.98	7.192

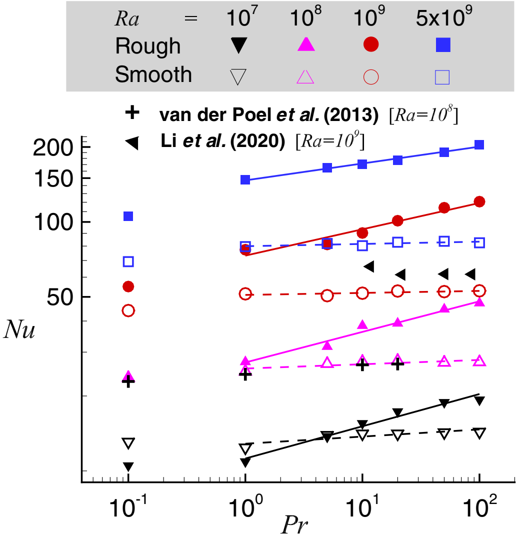

FIG. 2. The variation of Nu as a function of Pr is shown at different Ra for both the smooth and rough cells. Note that the power-law fit for Pr $\geqslant$ 1 is indicated by solid and dashed lines for rough and smooth cells, respectively.

$\phi(x, y, t)$ are used suitably such that $\langle\phi\rangle_t$ represents the time average, $\langle\phi\rangle_{V,t}$ implies the volume and time average, and $\langle\phi\rangle_{A,t}$ is the horizontal line and time average.

A. Nusselt number dependence on Ra and Pr

The scaling relation of the global heat transfer rate with imposed thermal forcing is at the heart of thermal convection. It is calculated as $\langle \mathrm{Nu}\rangle_{V,t} = \sqrt{\mathrm{Ra\,Pr}}\langle v\theta\rangle_{V,t} - \langle\partial_y\theta\rangle_{V,t}$. In Fig. 2, the Nusselt number dependence on Pr is explored for both the rough and smooth cells at different Ra. We observe that the heat transfer rate is lowest for Pr = 0.1. A distinct heat transport mechanism prevalent in the rough cell is manifested in the Nu(Pr) relation. For the smooth cell, Nu is invariant for Pr $\geqslant$ 1. This observation is in line with observations reported in various previous studies [7,16,18]. Also, for comparison, we have plotted the data of van der Poel *et al.* [18] and Li *et al.* [20]. It can be observed that the present data agree well with the reference data of van der Poel *et al.* [18] for a smooth cell of unit aspect ratio at Ra = 10^8 and $0.1 \leqslant \mathrm{Pr} \leqslant 20$. Also, the data of Li *et al.* [20] (quasi-2D study) exhibit weak Pr dependence (Ra = 10^9), but the value of Nu is slightly higher. The slightly higher value can be attributed to the quasi-2D nature of the problem as Nu is observed to have a higher value in 3D than in 2D [7,16,18]. In contrast to the trend followed by Nu(Pr) for the smooth cell, the heat transfer rate in the rough cell does not saturate for high-Pr flows. Here, higher Pr flows are seen to offer an augmented heat transfer rate. It is quite an interesting result, where the roughness configuration is seen to alter the role of Pr in the heat transfer process. Also, it is clearly evident that Nu in the rough cell is higher in comparison to the smooth cell except for the low-Pr cases at the lowest Ra = 10^7.

To establish a $\mathrm{Nu(Pr)} = A\mathrm{Pr}^m$ relation for Pr $\geqslant$ 1, the least-squares fitting is applied to the data. Note that the data for low Pr (<1) are not included because of the lack of enough data points to reveal the flow behavior, which is different from the flow behavior observed for moderate to large Pr flows. The details of the fitting parameters are listed in Table III for both the rough and smooth cells. It can be observed that the prefactor A is amplified with increasing Ra, whereas the scaling exponent m drops for both rough and smooth cells. Note that the scaling exponent m is a measure of how rapidly Nu varies with Pr. The drop in m with increasing Ra is an indicator of the declining

TABLE III. Prefactor and exponent of the least-squares fit $\mathrm{Nu(Pr)} = A\mathrm{Pr}^m$ at different Ra for $\mathrm{Pr} \geqslant 1$ for both the rough and smooth cells.

	Rough		Smooth	
Ra	A	m	A	m
10^7	11.215	0.129	12.856	0.029
10^8	27.267	0.123	25.775	0.017
10^9	73.247	0.106	50.919	0.008
5×10^9	146.91	0.067	79.896	0.009

effect of Pr on Nu for higher Ra. However, m being significantly higher for the rough case indicates that the state of Nu becoming invariant with respect to Pr is largely deferred in comparison to the smooth cell.

Next, the relation of Nu as a function of Ra is observed at different Pr. In Figs. 3(a) and 3(b), the Nusselt number variation as a function of Ra is presented for rough and smooth cells, respectively. Furthermore, the compensated plots of $\mathrm{Nu\,Ra}^{-1/3}$ for the rough cell and $\mathrm{Nu\,Ra}^{-2/7}$ for the smooth cell are shown as a function of Ra in Figs. 3(c) and 3(d), respectively. Note that the solid lines in Figs. 3(a) and 3(b) represent the power-law fitting to $\mathrm{Pr} = 0.1$, 1, and 100. The lines of best power fit are not shown for other Pr cases to avoid clutter. From Figs. 3(a) and 3(b), again, distinct Nu behavior in rough and smooth cells is evident. For the rough case, Nu exhibits Pr dependence.

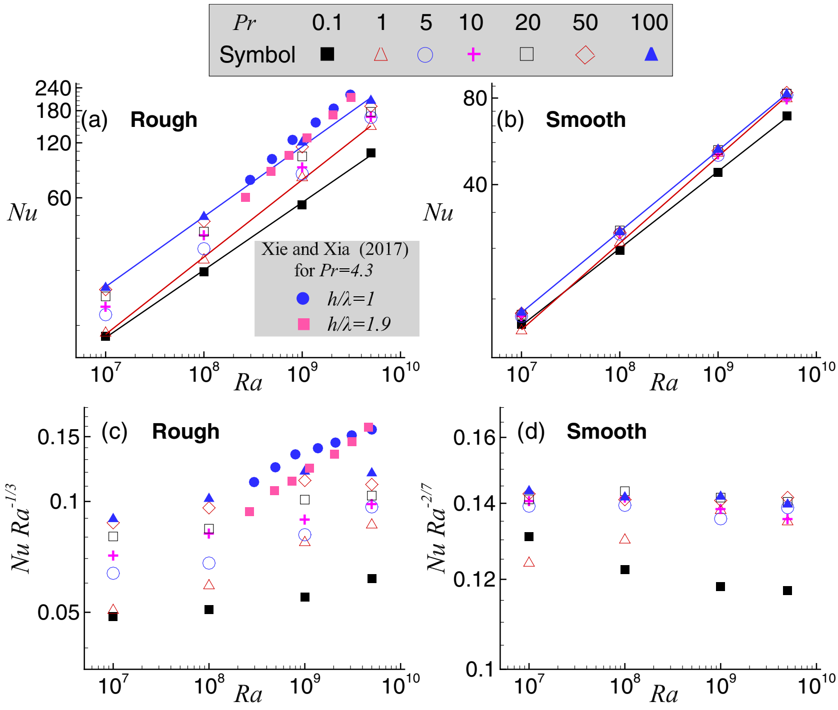

FIG. 3. In (a) and (b), Nu variation with Ra is shown at different Pr for the rough and smooth cells, respectively. Note that the solid lines representing the power-law fit are shown only for $\mathrm{Pr} = 0.1$, 1, and 100 to avoid clutter. The compensated plots of $\mathrm{Nu\,Ra}^{-1/3}$ and $\mathrm{Nu\,Ra}^{-2/7}$ as a function of Ra are shown in (c) and (d) for the rough and smooth cells, respectively. In (a) and (c), Nu data reported by Xie and Xia [31] for pyramidal roughness elements with $h/\lambda = 1$ and $h/\lambda = 1.9$ are also shown for comparison at $\mathrm{Pr} = 4.3$.

TABLE IV. Prefactor and exponent of the least-squares fit $\mathrm{Nu(Ra)} = B\mathrm{Ra}^n$ at different Pr for both the rough and smooth cells.

	Rough		Smooth	
Pr	B	n	B	n
0.1	0.026	0.37	0.171	0.268
1	0.012	0.423	0.097	0.301
5	0.021	0.4	0.144	0.284
10	0.032	0.384	0.157	0.279
20	0.038	0.379	0.145	0.284
50	0.044	0.377	0.145	0.284
100	0.040	0.383	0.152	0.282

For a higher Pr at a given Ra, a greater value of Nu is evident, whereas for the smooth case, Nu is nearly the same for $\mathrm{Pr} \geqslant 1$. To gain insights into the growth rate of Nu(Ra), the details of the scaling exponent and prefactor for $\mathrm{Nu(Ra)} = B\mathrm{Ra}^n$ are listed in Table IV . It can be observed that the scaling exponent n is least for $\mathrm{Pr} = 0.1$, while for $\mathrm{Pr} = 1$, it is highest (valid for both smooth and rough cells). Furthermore, it can be observed that the scaling exponent n is always higher for the rough cases at any Pr. For smooth surfaces, n assumes a value close to $2/7$. In the higher end of Pr, the scaling exponent n is observed to be nearly constant and invariant with respect to Pr in both cells. The compensated plots shown in Figs. 3(c) and 3(d) reveal how closely the scaling laws $\mathrm{Ra}^{1/3}$ and $\mathrm{Ra}^{2/7}$ are followed at different Pr for the rough and smooth cells, respectively. The flatter the data points are at a particular Pr, the better is their agreement with the perceived scaling exponent. From Fig. 3(d), it is evident that for the smooth cell, the scaling exponent of $n = 2/7$ is followed closely. However, the data points for the rough cell at a fixed Pr follow an increasing trend with the increasing Ra [see Fig. 3(b)], which reveals that n is higher than $1/3$. The above observations highlight that Pr assumes an active role in the presence of roughness in significantly enhancing the heat transfer rate in comparison to the smooth case, where Nu is lower and nearly invariant for moderate to large Pr. Furthermore, note that in Figs. 3(a) and 3(c), experimental Nu(Ra) data reported by Xie and Xia [31] for pyramidal-shaped roughness elements are shown for cases with aspect ratios $h/\lambda = 1$ and 1.9 of the roughness elements at $\mathrm{Pr} = 4.3$. Similar to our observation, they have also reported an augmented heat transfer scaling exponent in the presence of roughness. A higher value of the Nu scaling exponent is observed for a roughness configuration with a greater h/λ. van der Poel *et al.* [18], in their study involving a comparison of 2D and 3D results, reported a higher heat flux in 3D for the same input parameters, Ra and Pr. The lower Nu in the present 2D simulations compared with that reported by Xie and Xia [31] agrees well with the observation of van der Poel *et al.* [18].

Note that the scaling exponent obtained in this paper is greater than $1/3$ but the ultimate $1/2$ scaling is not realized. In contrast to the roughness studies by Zhu *et al.* [24] and Toppaladoddi *et al.* [22], where a scaling exponent close to $1/2$ is achieved, the roughness parameters (h and λ) are not optimized in this paper. Here, irregular roughness elements are incorporated such that there is no bias for any particular combination of h and λ. This highlights a possible reason for Nu scaling exponents deviating from $1/2$.

B. Flow topology and heat transfer mechanism

Prevalent flow structures in RBC have a close connection with the primary heat transfer mechanism. In addition to the applied thermal forcing, which is represented by Ra, the Prandtl number serves as an important input parameter that influences flow structures [4,5]. It is a widely accepted notion that in a rough convection cell, flow dynamics and structures are altered in comparison to a smooth convection cell [23,24,40,41], which enhances the heat transfer rate when thermal boundary layer thickness becomes comparable to the height of the rough surface. The efficacy of employing rough surfaces has recently been concluded to be dependent on thermal forcing [23]. For periodic rough surfaces, the enhanced heat transport scaling exponent ceases to exist at a higher Ra range when flow perturbations due to rough surfaces diminish. Efforts to prolong the propitious effect of rough surfaces in enhancing heat transfer led to the introduction of multiscale rough surfaces [24], which provided augmented heat transport for an even larger Ra range. The success of the multiscale surfaces at large thermal forcing is attributed to the thermal plumes triggered by small-scale elements. Till now, the majority of roughness studies have explored the response of a rough cell for varying Ra. However, there are only a few studies involving a rough cell that take into account the role of Pr in connection to the flow structures and heat transfer mechanism.

In Figs. 4(a)–4(i), snapshots of the instantaneous temperature field are shown for the rough cell for $\mathrm{Ra} = 10^8$, 10^9, and 5×10^9 at $\mathrm{Pr} = 0.1$, 10, and 100. The evolution of flow structures with increasing Ra and Pr can be observed from the temperature fields. For low $\mathrm{Pr} = 0.1$, a thick thermal boundary layer (TBL) over the rough surface is evident at $\mathrm{Ra} = 10^8$ [see Fig. 4(a)]. There are only a few plumes, which are of larger size, emanating mainly from the taller roughness elements. There is no significant contribution from small-scale elements as they are buried deep inside the thermal boundary layer, incapable of promoting plume emission. As Ra increases, the fluid layer of very high (low) temperature on the bottom (top) surface becomes thinner [see Figs. 4(d) and 4(g)]. This leads to an increased number of roughness elements now protruding into the TBL, the effect of which is evident in terms of a surge in plume nucleation sites. At $\mathrm{Ra} = 5 \times 10^9$, flow structures appear to be extremely fine and are highly localized. It can be observed that nearly all the roughness elements are involved in the plume nucleation and emission process.

It can be observed that for a given thermal forcing, an increase in Pr leads to the emergence of finer flow structures with a thinner TBL [see Figs. 4(b), 4(e), and 4(h)]. For $\mathrm{Pr} = 100$ [Figs. 4(c), 4(f), and 4(i)], there is strong clustering of fine mushroom-shaped plumes near the rough surfaces. It is interesting to note that for a thermal forcing as low as $\mathrm{Ra} = 10^8$ [Fig. 4(c)], plume emission sites are significantly higher for $\mathrm{Pr} = 100$ in comparison to lower-Pr cases [see Figs. 4(a)–4(c)]. The reason for the increased number of plume nucleation sites can be attributed to the activation of the small-scale roughness elements. The thinner TBL, in the case of large Pr, allows early activation of the small-scale elements. Hence stronger and increased flow perturbations are perceived in the flow at higher Pr even for a lower Ra. Another interesting observation is that though flow structures become finer with increasing Ra, they still manifest contrasting features for varied Pr. For instance, at the highest $\mathrm{Ra} = 5 \times 10^9$ and $\mathrm{Pr} = 100$, plumes are visibly finest and immensely localized in comparison to other Pr cases.

To compare the flow structures with a smooth convection cell for the same input parameters, we observe the snapshots of instantaneous temperature field data for the two extreme values of Pr (=0.1 and 100), as shown in Figs. 4(j)–4(o). The progression of large-scale flow structures into fine-scale intense structures is evident here also when either thermal forcing or Pr is increased. However, the intensity of the emitted plumes is relatively weaker than observed for the rough cells. Also, there is trivial plume-bulk interaction in contrast to the rough cells, where the localized emission of plumes, i.e., from the tips of the roughness elements, promotes better plume-bulk interaction. The existence of a strong temperature gradient at the tip of the roughness elements is responsible for the stimulation of intense plume emission. In line with the general expectation, it can be observed that bright detached flow structures (plumes) visibly span a larger portion of the convection cell for the roughened cells. The prominent presence of plumes in a rough cell, which are comparatively more energetic than those observed in a smooth cell, is an indication of enhanced heat transfer.

An estimate of the intensity of thermal plumes can be obtained by observing the mean instantaneous vertical velocity of the plumes. The procedure for demarcation of the fluid volumes into plume- or background-dominated regions is described in detail in Sec. III C. The mean vertical velocity v_{plm} is obtained by taking volume average of the absolute vertical velocity over the plume

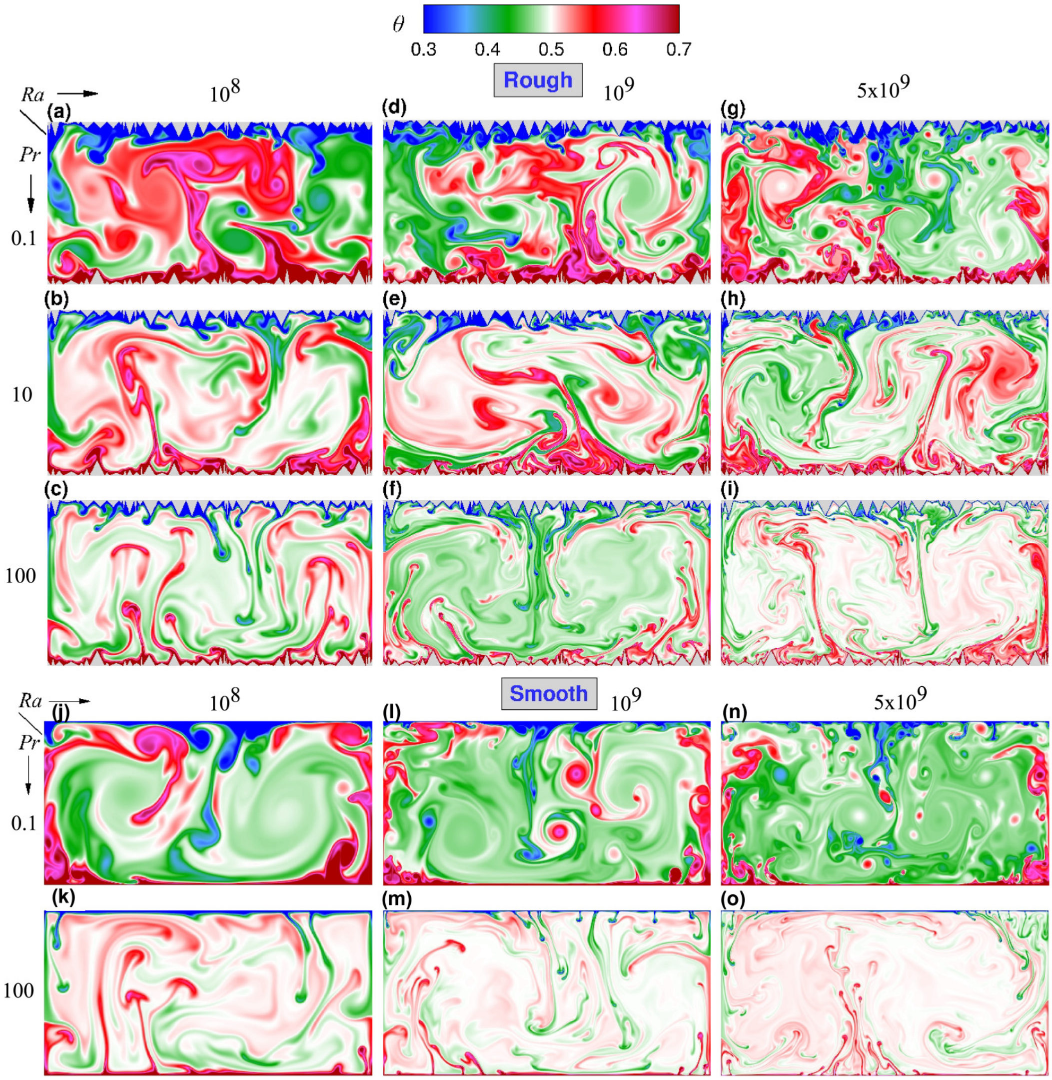

FIG. 4. (a)–(i) Snapshots of the instantaneous temperature field for the rough convection cell are shown at Ra $= 10^8$ [(a)–(c)], Ra $= 10^9$ [(d)–(f)], and Ra $= 5 \times 10^9$ [(g)–(i)] for Pr $= 0.1$, 10, and 100. (j)–(o) The temperature field is shown for the smooth cell at Ra $= 10^8$ [(j) and (k)], Ra $= 10^9$ [(l) and (m)], and Ra $= 5 \times 10^9$ [(n) and (o)] for the extreme values of Pr, Pr $= 0.1$ and Pr $= 100$.

regions as described below:

$$v_{plm} = \frac{1}{V_\Omega} \int_\Omega |v| dv \quad \text{such that } \Omega : |v'\theta'|/\Gamma' > \delta. \tag{4}$$

Note that Ω refers to the regions which satisfy the plume criterion, V_Ω is the volume of the plume regions, Γ' signifies the instantaneous global maximum of $|v'\theta'|$, and δ is the threshold parameter whose value is chosen as 5% for identifying plumes. In Fig. 5, v_{plm} is shown as a function of Pr at Ra $= 10^8$ and 5×10^9 for both smooth and rough cases. It can be observed that, in general, v_{plm} is comparable for the rough and smooth cases at Ra $= 10^8$. At a lower Ra, viscous forces remain largely stronger that hinder the emergence of the energetic plumes even from the rough

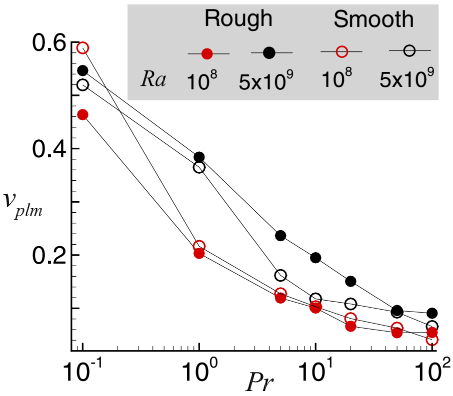

FIG. 5. The variation of the mean vertical velocity of plumes v_{plm} as a function of Pr is compared between the rough and smooth cells for $\mathrm{Ra} = 10^8$ and $\mathrm{Ra} = 5 \times 10^9$.

surfaces. For the flow at the lowest $\mathrm{Pr} = 0.1$, there is clearly a significant reduction in v_{plm} because of the formation of a thicker TBL, which obstructs not only the motion of flow inside the roughness cavities but also the formation of potent plumes. The true benefits of roughness are realized with the increase in thermal forcing, where the protrusion of roughness elements over the TBL yields stronger plumes and a greater number of plumes. The same is evident for 5×10^9, where v_{plm} is found to be significantly higher for the rough case. A higher v_{plm} serves as an indicator of the increased plume strength, which is realized with roughness at a higher thermal forcing.

C. Plume statistics

Thermal plumes are one of the most important flow structures that act as thermal carriers in transporting heat in the bottom-heated configuration. The introduction of rough surfaces is intimately linked to augmenting the emission of extra thermal plumes, which ultimately manifests in the form of enhanced heat transfer compared with the smooth case. To detect plume-dominated regions from the turbulent background, Emran and Schumacher [42] suggested that plumes are associated with a strong correlation between vertical velocity (v') and temperature (θ') fluctuations. Temperature fluctuation is calculated as $\theta'(\boldsymbol{x}, t) = \theta(\boldsymbol{x}, t) - \langle\theta(\boldsymbol{x})\rangle_{A,t}$, whereas vertical velocity fluctuation is defined as $v'(\boldsymbol{x}, t) = v(\boldsymbol{x}, t)$ as $\langle v\rangle_{A,t} = 0$. The criteria for detection of plume and background regions employed in this paper are modified as

$$V_{pl} = \boldsymbol{x} \in V : |v'\theta'|/\Gamma' > \delta, \quad V_{bg} = \boldsymbol{x} \in V : |v'\theta'|/\Gamma' \leqslant \delta. \tag{5}$$

Here, V_{pl} and V_{bg} represent the volume fractions of plume- and background-dominated regions, respectively, Γ' is the instantaneous global maximum of $|v'\theta'|$, and δ is a free parameter controlling the threshold scale. Note that to account for the previously ignored yet significant anomalous motion of the plumes, i.e., the downward motion of hot plumes or upward motion of cold plumes, the absolute value of $|v'\theta'|$ is used as opposed to the signed correlation proposed by Emran and Schumacher [42]. This provision is important as a 2D configuration lacks an extra direction for the fluid to escape. This explains the need to incorporate the nonintuitive motion of plumes. If the conventional plume detection method is used, then plumes exhibiting anomalous motion, in other words, negative $v'\theta'$, go undetected and are misinterpreted as background regions.

In Fig. 6, the variation of volume fractions of plume (V_{pl}) and background (V_{bg}) regions as a function of Ra is shown for different Pr at thresholds $\delta = 5$ and 10%. Note that the two different thresholds both identify plumes reasonably well and are used to see their effect on the volume fractions. It can be observed that for all Pr cases, irrespective of δ, V_{pl} drops with increasing Ra, while V_{bg} climbs in order to compensate for the diminishing V_{pl}. The results are in agreement with

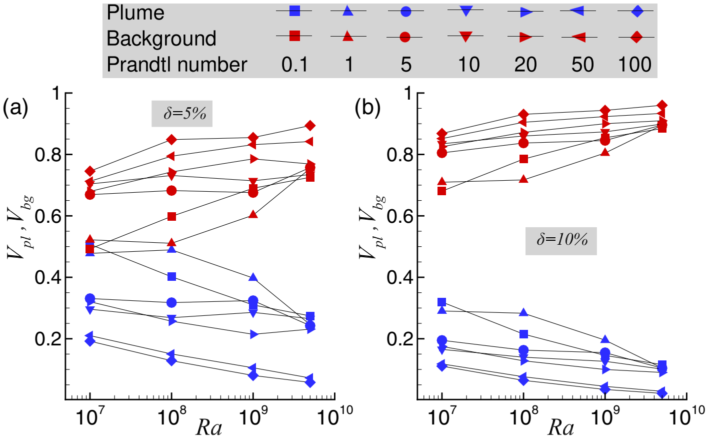

FIG. 6. The variation of the volume fraction of plumes (V_{pl}) and background (V_{bg}) as a function of Ra is explored for different Pr at thresholds (a) $\delta = 5\%$ and (b) $\delta = 10\%$ for the rough cell.

the general consensus that the higher the thermal forcing is, the greater are the extent and role of the turbulent background. Note that in general, the higher the Pr is, the smaller is the value of V_{pl}, which is in line with the observation that plume structures emerge as finer structures as Pr is increased and are likely to cover a relatively smaller fraction of the cell volume.

The increased plume emission in the rough case is expected to exhibit a higher V_{pl} than its smooth counterpart. In Fig. 7, a direct comparison is made between V_{pl} of smooth and rough cells for different Pr as a function of Ra at $\delta = 5$ and 10%. It is clearly evident that the rough cases have significantly higher V_{pl} for all Pr when $\mathrm{Ra} \geqslant 10^8$. At $\mathrm{Ra} = 10^7$ and $\mathrm{Pr} = 0.1$ and 1, the heat transfer rate remains comparable in the two types of cells. However, for $\mathrm{Pr} = 50$ and 100, Nu is significantly higher in the rough cases. At the lower Pr, owing to a thicker TBL, fluid is stuck inside the cavities and is unable to effect perturbations in the flow, which explains the inability of a rough cell to augment the heat transfer. However, at a higher Pr, a greater number of roughness elements introduce perturbations in the system because of a thinner TBL, which ultimately yields a larger Nu.

Furthermore, the variation of thermal dissipation, $\varepsilon_\theta = (\mathrm{Ra}\,\mathrm{Pr})^{-1/2}|\nabla\theta|^2$, contributed by the plume (ε_{pl}) and background (ε_{bg}) regions with Ra is explored in Fig. 8, for different Pr at $\delta = 5$

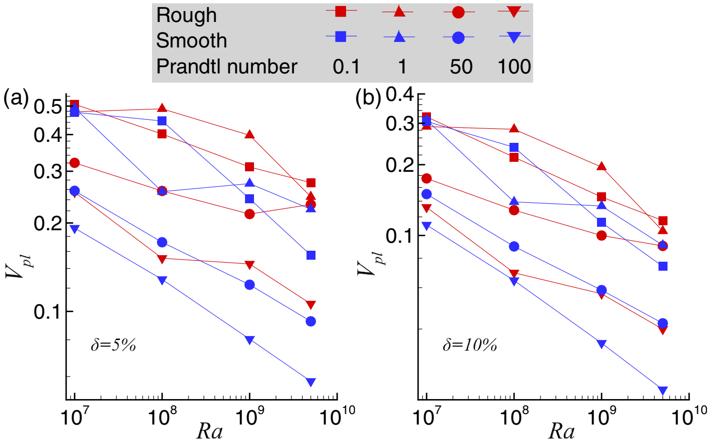

FIG. 7. The plume volume fraction V_{pl} as a function of Ra is compared between the rough and smooth cells for different Pr at (a) $\delta = 5\%$ and (b) $\delta = 10\%$.

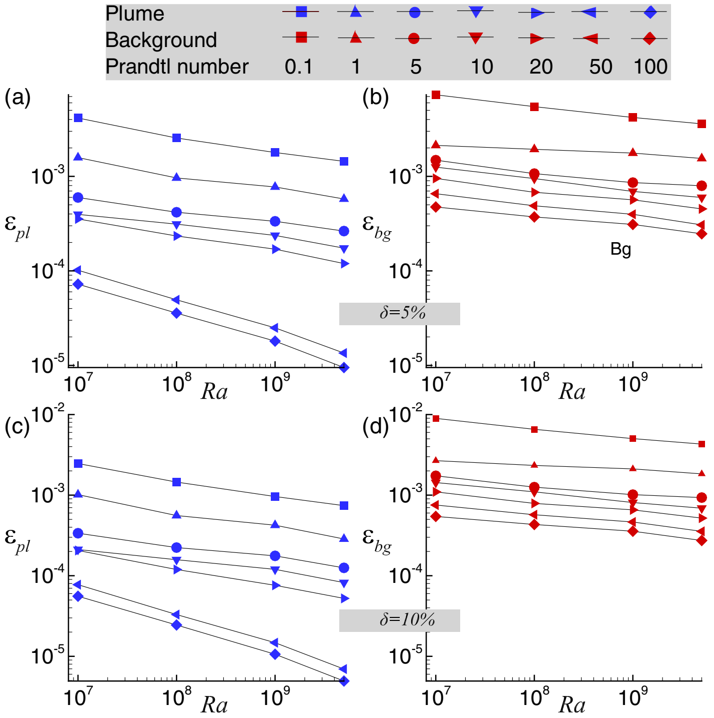

FIG. 8. The thermal dissipation contributions from plumes (ε_{pl}) and background (ε_{bg}) are shown as a function of Ra at different Pr. The top row shows the data based on the $\delta = 5\%$ criterion, while for the bottom row, δ is 10%. Note that (a) and (c) show data for ε_{pl}, while (b) and (d) represent data for ε_{bg}.

and 10%. The dissipation contributions are calculated as

$$\varepsilon_{pl} = \left\langle \int_{V_{pl}} \varepsilon_\theta(\boldsymbol{x}, t) dV \right\rangle_t \quad \text{and} \quad \varepsilon_{bg} = \left\langle \int_{V_{bg}} \varepsilon_\theta(\boldsymbol{x}, t) dV \right\rangle_t ,$$

where $\varepsilon_\theta(\boldsymbol{x}, t)$ is the local nondimensional thermal dissipation rate. We observe that plume and background regions tend to contribute less to ε_θ as Ra is increased. The same is evident from the monotonic decrease in both ε_{pl} and ε_{bg} with increasing Ra for all Pr. Note that the decay of the net thermal dissipation rate ($\varepsilon_{pl} + \varepsilon_{bg}$) is in accordance with the exact relation $\langle \varepsilon_\theta \rangle_V = \langle \mathrm{Nu} \rangle_V / \sqrt{\mathrm{Ra\,Pr}}$. For a fixed thermal forcing, a lower-Pr flow exhibits higher ε_{pl} and ε_{bg}, while they drop significantly as Pr increases. Another observation is that irrespective of δ or Pr, ε_{bg} is higher than ε_{pl}. It is a general expectation that a higher V_{bg} should yield a higher ε_{bg}. Now, if we refer to Fig. 6, it can be readily observed that V_{bg} exceeds V_{pl} almost for all cases irrespective of δ, which explains the perceived dominance of ε_{bg}. Also, a direct comparison between smooth and rough cells is made for ε_{pl} as a function of Ra and Pr at $\delta = 5$ and 10%, as shown in Fig. 9. It can be observed that in line with the higher V_{pl} in the rough cell, ε_{pl} is found to be substantially higher in the rough cell than in the smooth cell at all Ra and Pr. Note that the decay rate of ε_{pl} in the rough cell is smaller than that observed for the smooth cell. This essentially highlights that the extra plume contributions received from roughness elements are sustained for the entire explored Ra range.

D. Reynolds number dependence on Ra and Pr

The flow strength developed in the convection cell due to the applied thermal forcing exhibits a strong dependence on the type of fluid used and has close links to the heat transport process. The

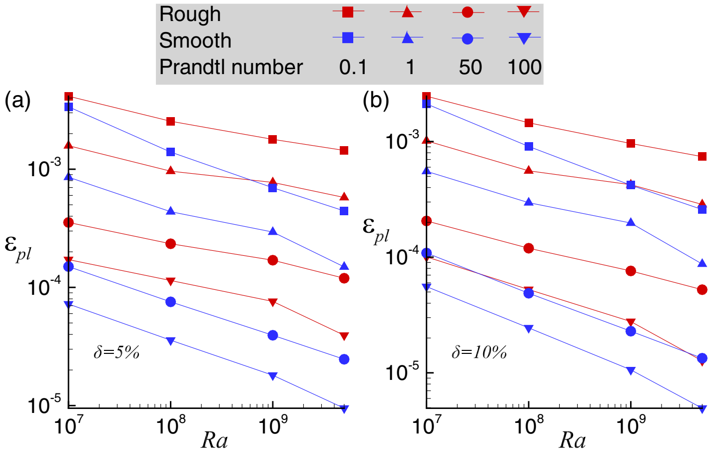

FIG. 9. The variation of ε_{pl} as a function of Ra is compared between the rough and smooth cells at different Pr based on (a) $\delta = 5\%$ and (b) $\delta = 10\%$.

intensity of the flow is usually described in terms of the Reynolds number [18,29], which can be quantified as

$$\mathrm{Re} = \sqrt{\langle \boldsymbol{u} \cdot \boldsymbol{u} \rangle_{V,t}\, \mathrm{Ra}/\mathrm{Pr}}.$$

In Fig. 10 , the Reynolds number dependence on Pr is shown for both smooth and rough cells at different Ra. It can be observed that for a fixed Pr, a higher Ra yields a stronger flow strength. However, for a fixed Ra, increasing Pr is seen to attenuate the flow intensity. Upon comparing Re between smooth and rough cells, enhanced flow strength in the rough cell is clearly evident for $10^8 \leqslant \mathrm{Ra} \leqslant 5 \times 10^9$ and $5 \leqslant \mathrm{Pr} \leqslant 100$. For lower Pr = 0.1 and 1, the enhancement of Re due to rough surfaces is observed only in the higher Ra range ($\geqslant 10^9$). The reason for not realizing an enhanced Re for lower Ra is associated with the immobility of fluid inside the cavities, where the flow is largely viscosity dominated. However, at higher Pr, owing to the thinner TBL, cavity regions are easily ventilated by the bulk flow, promoting stronger fluid motion, which is responsible for an

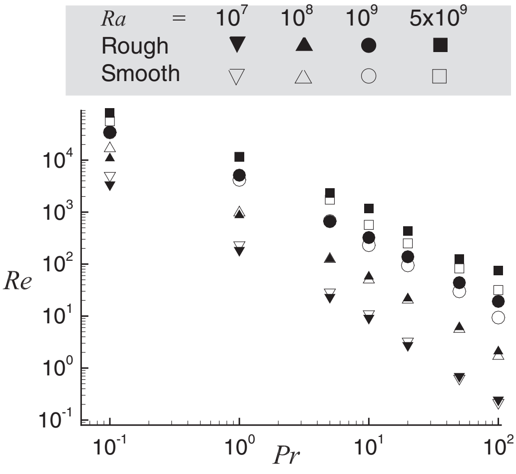

FIG. 10. The Re dependence on Pr is explored for different thermal forcings in rough and smooth cells.

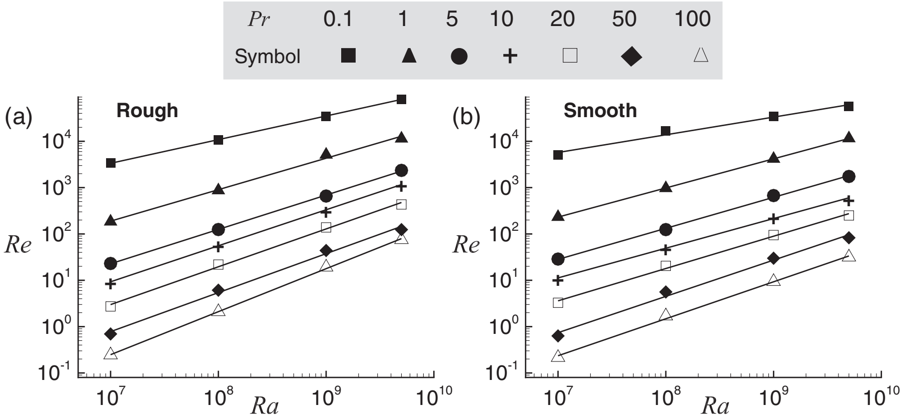

FIG. 11. The variation of Re with Ra is shown at different Pr for (a) rough and (b) smooth cells. Note that the solid black lines correspond to the least-squares fit to the data.

increased Re. Note that contrary to our previous observation that Nu loses its dependence on Pr in the smooth cell, Re(Pr) dependence is not lost in either of the cells.

In Fig. 11, Re dependence on Ra is observed for both the rough and smooth cell configurations. The increasing trend of Re with Ra is clearly evident here for both the smooth and rough configurations. From Fig. 11, it is easy to observe that at the highest value of Ra, $\mathrm{Ra} = 5 \times 10^9$, a higher Re exists for the rough cell at all Pr when compared with the smooth cell. To establish a relation of the form $\mathrm{Re(Ra)} = A\mathrm{Ra}^n$, we have applied the least-squares fitting to the data. The details of the scaling exponent and prefactor are listed in Table V. In general, it can be observed that the scaling exponent n increases as Pr is increased, while the prefactor A diminishes with Pr in both the cells. Most importantly, at any fixed Pr, n is higher for the rough cells. The increased exponent highlights that the flow strength is largely influenced by the introduction of rough surfaces.

IV. SUMMARY AND CONCLUSIONS

This paper attempts to find the role of Pr in influencing flow structures and the prevalent heat transport mechanism in a two-dimensional rough rectangular convection cell. We show the importance of the choice of fluid, in addition to the applied temperature forcing, in realizing an augmented heat transfer rate from the roughened cell. The distinct role played by Pr in the presence of roughness is evident in the form of a monotonic increase in Nu with increasing Pr. The result is

TABLE V. Prefactor and exponent of the least-squares fit $\mathrm{Re(Ra)} = A\mathrm{Ra}^n$ at different Pr for both the rough and smooth cells.

	Rough		Smooth	
Pr	A	n	A	n
0.1	0.895	0.51	12.176	0.382
1	3.358×10^{-3}	0.679	9.158×10^{-3}	0.629
5	1.477×10^{-4}	0.741	5.798×10^{-4}	0.670
10	3.377×10^{-5}	0.777	3.708×10^{-4}	0.640
20	5.764×10^{-6}	0.816	4.751×10^{-5}	0.697
50	1.007×10^{-6}	0.841	2.458×10^{-6}	0.783
100	7.937×10^{-8}	0.928	6.119×10^{-7}	0.798

a significant improvement compared with the nearly invariant Nu observed in the smooth cell. At a lower Pr, a thick layer of hot (cold) fluid is observed above the top (bottom) plate, while a higher Pr is associated with a thinner thermal boundary layer (TBL). For the former, large-scale diffuse structures are prevalent, while for the latter, fine mushroom-shaped structures are discharged from the near-wall regions. At a lower Ra, since roughness elements are embedded beneath the TBL, plume emission from them is thwarted. The creation of numerous nucleation sites and subsequent frequent plume emission are observed at higher Pr as more and more roughness elements puncture the TBL. At a given Ra, since a high-Pr flow boasts a thinner TBL, roughness elements become thermally active quickly. This results in augmented Nu at higher Pr.

In comparison to the smooth case, plumes are observed to span a wider extent of the domain in the rough cell. Also, they are more localized and intense, which finally yields greater heat transport. A comparison of the mean vertical velocity of plumes in smooth and rough cells at a sufficiently high thermal forcing corroborates the finding that roughness-facilitated plumes are more energetic. At a lower $\mathrm{Ra} = 10^8$, where viscous force dominates, mean plume vertical velocities corresponding to rough and smooth cells are comparable though a higher fraction of plumes is recorded in the rough configuration. The level of flow perturbations effected by rough surfaces can be controlled by either increasing Ra or increasing Pr or both. A direct comparison of flow intensity measured in terms of the global Reynolds number between rough and smooth cells reveals that Re is superior for the rough cell for a larger Ra or Pr. The diminished flow intensity for extremely low Ra or Pr can be attributed to the entrapment of fluid inside the roughness cavities, where the flow is largely viscosity dominated.

The data that support the findings of this study are available from the corresponding author upon reasonable request.

ACKNOWLEDGMENTS

The research was completed using the funds provided for SERB Project No. CRG/2019/000177. All the simulations were computed in Param-Ishan, the supercomputing facility at Indian Institute of Technology Guwahati (IITG)

The authors report no conflict of interest.

APPENDIX: DETAILS OF NUMERICAL SETUP

1. Comparison tests

The results reported by Zhu *et al.* [23] for sinusoidal roughness on horizontal plates with both h/H and λ/H being 0.1 are reproduced in Fig. 12 to check the capability of the present numerical setup. It can be seen from Fig. 12(a) that Nu(Ra) agrees well with an average and maximum

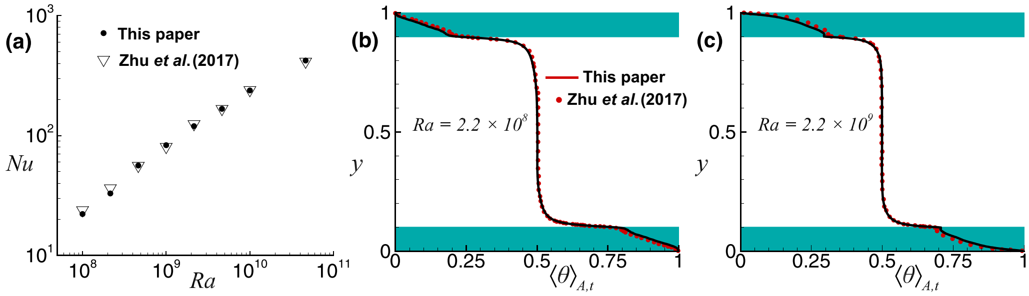

FIG. 12. (a) The mean Nu(Ra) and (b) and (c) vertical mean temperature ($\langle\theta\rangle_{A,t}$) profiles for the sinusoidal roughness ($h = \lambda = 0.1$) are compared with the corresponding data obtained by Zhu *et al.* [23]. Note that the height of the shaded portions indicates the amplitude of the roughness elements.

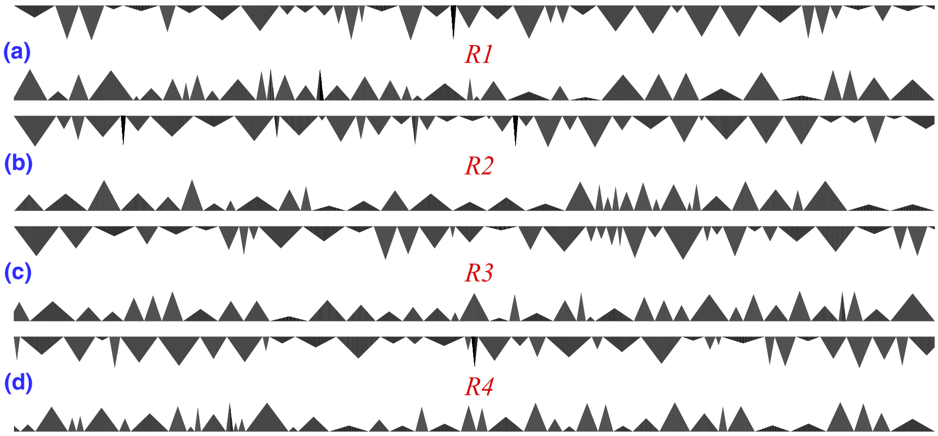

FIG. 13. Schematics showing the rough surfaces used on the top and bottom plates for the different flow realizations (a) $R1$, (b) $R2$, (c) $R3$, and (d) $R4$ at $\mathrm{Ra} = 1.5 \times 10^9$.

variation of 3 and 7%, respectively, which is reasonable given the complexity of the problem, the difference in the numerical methods, and the large range of Nu data. In Figs. 12(b) and 12(c), we show vertical mean temperature profiles for $\mathrm{Ra} = 2.2 \times 10^8$ and 2.2×10^9, respectively. It can be observed that the profiles compare accurately with the reference data, which highlights the effectiveness of the present setup in handling rough surfaces.

2. Mean Nu for different flow realizations

To determine whether different flow realizations (R_1, R_2, R_3, and R_4) corresponding to different distributions of roughness elements yield a converged mean Nusselt number, we have simulated the flow at $\mathrm{Ra} = 1.5 \times 10^9$ and $\mathrm{Pr} = 0.7$. Figure 13 shows the roughness elements used on the horizontal plates for different flow realizations. Note that the admissible range for variation of amplitude and width of roughness elements (1–10% of H) is kept the same in all the realizations. In Table VI, the details of the mean Nusselt number corresponding to different realizations are listed along with the wetted area of the rough surfaces. It can be observed that $\langle \mathrm{Nu} \rangle_{V,t}$ converges quite well such that the maximum variation between any two realizations does not exceed 2.1%.

3. Near-wall resolution

To ensure adequate resolution of the rough elements, a sufficiently fine grid close to the walls is used. Figures 14(a)–14(c) show the grid resolution for three roughness elements of extreme dimensions at $\mathrm{Ra} = 10^8$. It can be seen that the elements contain a sufficient number of cells to resolve them. The excellent resolution of the rough surface is further reflected from the volume

TABLE VI. Global Nusselt number for different realizations at $\mathrm{Ra} = 1.5 \times 10^9$ along with the total wetted area A_{wet} of the rough surfaces.

Realization	$\langle \mathrm{Nu} \rangle_{V,t}$	A_{wet}
R_1	96.05	10.01
R_2	95.74	9.74
R_3	94.04	9.64
R_4	94.80	10.19

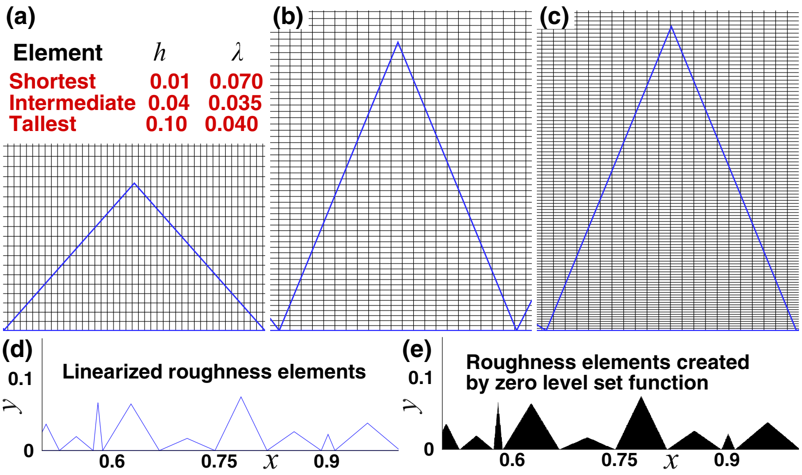

FIG. 14. In (a)–(c), the mesh resolution for three extreme roughness elements on the bottom plate is shown at $\mathrm{Ra} = 10^8$. From (a) to (b) to (c), the height of the elements increases. Also, note that (a)–(c) do not follow the same scale. In (d), a segment of the bottom rough surface created using the linearized elements is shown, whereas (e) illustrates the reconstruction of the surface using the zero level set function.

rendering of the zero level set function [33,36,43] shown in Fig. 14(e), which matches perfectly with the exact linearized object [see Fig. 14(d)]. The errors in the reconstruction of the exact roughness volume are 0.07 and 0.005% for the coarsest and finest meshes used in this paper, respectively.

[1] E. Bodenschatz, W. Pesch, and G. Ahlers, Recent developments in Rayleigh-Bénard convection, Annu. Rev. Fluid Mech. **32**, 709 (2000).

[2] F. Chilla and J. Schumacher, New perspectives in turbulent Rayleigh-Bénard convection, Eur. Phys. J. E: Soft Matter Biol. Phys. **35**, 58 (2012).

[3] G. Ahlers, S. Grossmann, and D. Lohse, Heat transfer and large scale dynamics in turbulent Rayleigh-Bénard convection, Rev. Mod. Phys. **81**, 503 (2009).

[4] S. Grossmann and D. Lohse, Scaling in thermal convection: a unifing theory, J. Fluid Mech. **407**, 27 (2000).

[5] S. Grossmann and D. Lohse, Thermal Convection for Large Prandtl Numbers, Phys. Rev. Lett. **86**, 3316 (2001).

[6] G. Silano, K. R. Sreenivasan, and R. Verzicco, Numerical simulations of Rayleigh-Bénard convection for Prandtl numbers between 10^{-1} and 10^4 and Rayleigh numbers between 10^5 and 10^9, J. Fluid Mech. **662**, 409 (2010).

[7] R. Verzicco and R. Camussi, Prandtl number effects in convective turbulence, J. Fluid Mech. **383**, 55 (1999).

[8] A. V. Malevsky, Patterns of convective turbulence: An effect of Prandtl number, Phys. Earth Planet. Inter. **88**, 31 (1995).

[9] V. Yakhot, Probability Distributions in High-Rayleigh Number Bénard Convection, Phys. Rev. Lett. **63**, 1965 (1989).

[10] T. H. Solomon and J. P. Gollub, Sheared Boundary Layers in Turbulent Rayleigh-Bénard Convection, Phys. Rev. Lett. **64**, 2382 (1990).

[11] T. H. Solomon and J. P. Gollub, Thermal boundary layers and heat flux in turbulent convection: The role of recirculating flows, Phys. Rev. A **43**, 6683 (1991).

[12] A. M. Obukhov, On the influence of Archimedean forces on the structure of the temperature field in a turbulent flow, Dokl. Akad. Nauk. SSR **125**, 1246 (1959).

[13] R. Bolgiano, Turbulent spectra in a stably stratified atmosphere, J. Geophys. Res. **64**, 2226 (1959).

[14] A. Brandenburg, Energy Spectra in a Model for Convective Turbulence, Phys. Rev. Lett. **69**, 605 (1992).

[15] M. Lesieur, *Turbulence in Fluids* (Martinus Nijhoff, Dordrecht, 1987).

[16] Y. X. Huang and Q. Zhou, Counter-gradient heat transport in two-dimensional turbulent Rayleigh-Bénard convection, J. Fluid Mech. **737**, R3 (2013).

[17] Y.-H. Yang, X. Zhu, B.-F. Wang, Y.-L. Liu, and Q. Zhou, Experimental investigation of turbulent Rayleigh-Bénard convection of water in a cylindrical cell: The Prandtl number effects for $Pr > 1$, Phys. Fluids **32**, 015101 (2020).

[18] E. P. van der Poel, R. J. A. M. Stevens, and D. Lohse, Comparison between two-and three-dimensional Rayleigh-Bénard convection, J. Fluid Mech. **736**, 177 (2013).

[19] A. Pandey, M. K. Verma, A. G. Chatterjee, and B. Dutta, Similarities between 2D and 3D convection for large Prandtl number, Pramana - J. Phys. **87**, 13 (2016).

[20] X.-M. Li, J.-D. He, Y. Tian, P. Hao, and S.-D. Huang, Effects of Prandtl number in quasi-two-dimensional Rayleigh-Bénard convection, J. Fluid Mech. **915**, A60 (2021).

[21] Y. Zhang, C. Sun, Y. Bao, and Q. Zhou, How surface roughness reduces heat transport for small roughness heights in turbulent Rayleigh-Bénard convection, J. Fluid Mech. **836**, R2 (2018).

[22] S. Toppaladoddi, S. Succi, and J. S. Wettlaufer, Roughness as a Route to the Ultimate Regime of Thermal Convection, Phys. Rev. Lett. **118**, 074503 (2017).

[23] X. Zhu, R. J. A. M. Stevens, R. Verzicco, and D. Lohse, Roughness Facilitated Local 1/2 Scaling Does Not Imply the Onset of the Ultimate Regime of Thermal Convection, Phys. Rev. Lett. **119**, 154501 (2017).

[24] X. Zhu, R. J. A. M. Stevens, O. Shishkina, R. Verzicco, and D. Lohse, $Nu \sim Ra^{1/2}$ scaling enabled by multiscale wall roughness in Rayleigh-Bénard turbulence, J. Fluid Mech. **869**, R4 (2019).

[25] S. Toppaladoddi, A. J. Wells, C. R. Doering, and J. S. Wettlaufer, Thermal convection over fractal surfaces, J. Fluid Mech. **907**, A12 (2021).

[26] R. H. Kraichnan, Turbulent thermal convection at arbitrary Prandtl number, Phys. Fluids **5**, 1374 (1962).

[27] E. A. Speigel, Convection in stars I. Basic Boussinesq convection, Annu. Rev. Astron. Astrophys. **9**, 323 (1971).

[28] K. Chand, M. Sharma, and A. K. De, Significance of near-wall dynamics in enhancement of heat flux for roughness aided turbulent Rayleigh-Bénard convection, Phys. Fluids **33**, 065114 (2021).

[29] Y. Zhang, Q. Zhou, and C. Sun, Statistics of kinetic and thermal energy dissipation rates in two-dimensional turbulent Rayleigh-Bénard convection, J. Fluid Mech. **814**, 165 (2017).

[30] D.-L. Dong, B.-F. Wang, Y.-H. Dong, Y.-X. Huang, N. Jiang, Y.-L. Liu, Z.-M. Lu, X. Qiu, Z.-Q. Tang, and Q. Zhou, Influence of spatial arrangements of roughness elements on turbulent Rayleigh-Bénard convection, Phys. Fluids **32**, 045114 (2020).

[31] Y. C. Xie and K. Q. Xia, Turbulent thermal convection over rough plates with varying roughness geometries, J. Fluid Mech. **825**, 573 (2017).

[32] J. L. Yang, Y. Z. Zhang, T. C. Jin, Y. H. Dong, B. F. Wang, and Q. Zhou, The Pr-dependence of the critical roughness height in two-dimensional turbulent Rayleigh-Bénard convection, J. Fluid Mech. **911**, A52 (2021).

[33] A. K. De, A diffuse interface immersed boundary method for complex moving boundary problems, J. Comput. Phys. **366**, 226 (2018).

[34] S. Peter and A. K. De, Wake instability modes for forced transverse oscillation of a sphere, Ocean Eng. **115**, 48 (2016).

[35] A. K. De, V. Eswaran, and P. K. Mishra, Dynamics of plumes in turbulent Rayleigh-Bénard convection, Eur. J. Mech. B Fluids **72**, 164 (2018).

[36] A. K. De and S. Sarkar, Three-dimensional wake dynamics behind a tapered cylinder with large taper ratio, Phys. Fluids **32**, 063604 (2020).

[37] K. Chand, A. K. De, and P. K. Mishra, Enhanced heat flux and flow structures in turbulent Rayleigh-Bénard convection with rough boundaries, Phys. Rev. Fluids **6**, 124605 (2021).

[38] A. K. De and S. Sarkar, Dependence of wake structure on pitching frequency behind a thin panel at $Re = 1000$, J. Fluid Mech. **924**, A33 (2021).

[39] A. K. De and S. Sarkar, Spatial wake transition past a thin pitching plate, Phys. Rev. E **104**, 025106 (2021).

[40] Y. B. Du and P. Tong, Enhanced Heat Transport in Turbulent Convection over a Rough Surface, Phys. Rev. Lett. **81**, 987 (1998).

[41] Y. B. Du and P. Tong, Turbulent thermal convection in a cell with ordered rough boundaries, J. Fluid Mech. **407**, 57 (2000).

[42] M. S. Emran and J. Schumacher, Conditional statistics of thermal dissipation rate in turbulent Rayleigh-Bénard convection, Eur. Phys. J. E: Soft Matter Biol. Phys. **35**, 108 (2012).

[43] A. K. De, A diffuse interface immersed boundary method for convective heat and fluid flow, Int. J. Heat Mass Transfer **92**, 957 (2016).